

MORPHOLOGY OF GRAPHITE AGGLOMERATES OBTAINED BY SPHERICAL AGGLOMERATION VIA PROPAGATION-BASED X-RAY MICROTO- MOGRAPHY

JULIA SCHREIER✉ AND ULRICH BRÖCKEL

University of Applied Sciences Trier, Institute for Micro-Process-Engineering and Particle Technology (IMiP), Umwelt-Campus Birkenfeld, P.O. Box 1380, D-55761 Birkenfeld, Germany
e-mail: j.schreier@umwelt-campus.de; u.broeckel@umwelt-campus.de

(Received July 11, 2023; revised February 9, 2024; accepted February 11, 2024)

ABSTRACT

The aim of this work was to develop a novel method for studying the 3D morphology of agglomerates obtained by spherical agglomeration. It has been found, that the combination of shock-freezing the samples in a mixture of ethanol and dry ice followed by an X-ray microtomography measurement leads to useful results. Hereby, the image quality for low absorbing material like the used graphite was enhanced by propagation-based X-ray microtomography, which results in phase contrast images. We also discuss our 3D image post-processing routine, which is used to determine the morphology parameters sphericity, fractal dimension and packing density. Furthermore, a two-dimensional kernel density estimation is used to calculate the joint probability density of agglomerate size and the morphology parameter. In future, this method will be used to determine the morphological behaviour of agglomerates during the different phases of spherical agglomeration.

Keywords: morphology, phase-contrast, spherical agglomeration, two-dimensional characterisation, X-ray microtomography.

INTRODUCTION

Spherical agglomeration, or agglomeration in liquids, has been used for more than 100 years, as Cattermole's (1904) patent shows. Fundamentally, spherical agglomeration consists of a three-phase system (suspension liquid / particles / binding liquid) and is conducted in a stirred vessel. Typical particle sizes range from 0.1 μm up to several 100 μm according to various studies (Dawei *et al.*, 1986; Drzymala *et al.*, 1991; House and Veal, 1989; Kelsall and Pitt, 1987; Petela *et al.*, 1995; Sirianni *et al.*, 1969; Wahl and Baker, 1971) with water commonly used as suspension liquid. Additionally, the binding liquid must fulfil two requirements; being immiscible with the suspension liquid and preferably wetting the suspended particles.

Several studies have investigated the kinetics of the spherical agglomeration process, including Bemmerl (1979), Bos (1983), Kawashima & Capes (1974; 1976), and Kawashima *et al.* (1981). The process consists of three distinct phases. Following the addition of binding liquid to the particle-water-suspension, the agglomeration process is initiated. In the beginning, particles and binding liquid droplets collide due to turbulent mixing through the stirrer. When the binding liquid meets the

requirement to preferentially wet the suspended particles, the binding liquid droplets and the particles stick together after the collision. Depending on the size of the collision partners, the outcome is either a droplet covered with particles or a wetted particle. Over time, and through the power input of the stirrer, the wetted particles stick together due to capillary forces and creating microagglomerates. This initial stage is known as the wetting phase.

The formation of microagglomerates is optically detectable by clarification of the turbid suspension, which was first described by Bos (1983). Turbidity decreases during the beginning of the fast growth regime, which is the second process phase. Furthermore, agglomerate size rapidly increases until reaching equilibrium after which no further growth occurs.

During spherical agglomeration, these three process phases can also be monitored by measuring the stirrer torque. In the early stages of agglomeration, the torque is stable. As the turbidity of the suspension decreases, the torque also decreases. After reaching a minimum, the torque then increases towards another stable plateau. These phenomena were first published by Kawashima &

Capes (1976) and in a previous study published by Schreier & Bröckel (2021).

The aim of this paper is to present a method to examine the agglomerate morphology during the agglomeration process. This approach will be the basis for understanding the torque behaviour mentioned above. There are a few publications in the literature characterising the morphology of agglomerates obtained by spherical agglomeration via either scanning electron microscopy (SEM) or optical microscopy coupled with 2D image analysis (Thati and Rasmuson, 2012, Kardos *et al.*, 2016; Guo *et al.*, 2022;). The morphological parameters of 2D imaging depend on orientation of the object. This limitation can be overcome by using X-ray microtomography (μ CT) in combination with 3D image analysis (Miller and Lin, 2004; Gilson and Bröckel, 2015; Dioguardi *et al.*, 2017; Dosta *et al.*, 2018; Leißner *et al.*, 2019; Schreier and Bröckel, 2021). Other studies have also been done to characterise the morphology of agglomerates using μ CT, e.g. agglomerates produced by spray fluidised bed (Pashminehazar *et al.*, 2016; 2018). All these experiments have in common that they characterise the morphology at the end of the process.

In our study, our objective is to analyse the agglomerate morphology over the entire spherical agglomeration in the future. To achieve this goal, we use a specific sample preparation that minimises the influence on the morphology of two exemplary samples (after 30 s & 150 s agglomeration time), but is also stable enough for the μ CT measurement (see section Sample Preparation for μ CT). Another objective is to illustrate the image post-processing routine used to obtain the morphological parameters on these exemplary samples (see section Image Processing & Analysis Routine). Furthermore, the object discrete data obtained by 3D image analysis can be used to calculate the joint two-dimensional number-based probability density distributions by two-dimensional kernel density estimation (see section Two-dimensional Kernel Density Distribution). This distribution type offers a better insight into the dependence of the analysed parameters on each other, e.g. the size dependence of the individual morphological parameters.

PROPAGATION-BASED X-RAY MICROCTOGRAPHY

The basic setup of a laboratory μ CT is illustrated in Fig. 1 and consists of a cone beam X-ray source, a rotationally symmetric sample, and a CCD camera as detector.

During the measurement, the sample rotates around its axis in pre-defined angular steps, each time taking a projection image. This set of projection images serves as

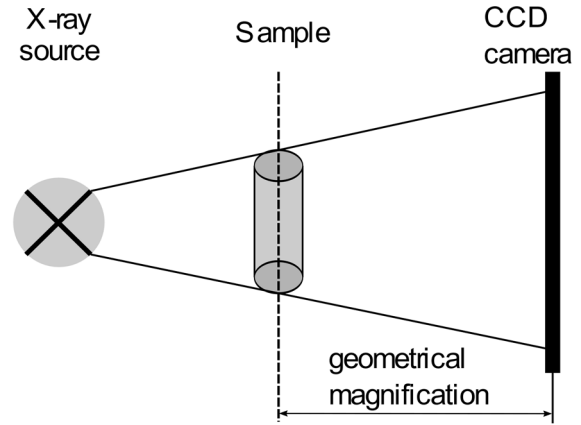


Fig. 1. μ CT setup.

the input for the subsequent reconstruction algorithm, which transforms the dataset into a 3D representation of the sample.

Generally, X-rays interacting with material can be described by the complex refractive index n (Eq. (1)), where δ denotes the phase shift of the X-ray wave, causing deviation from the initial direction, while β stands for X-ray absorption

$$n = 1 - \delta + i\beta. \quad (1)$$

In traditional μ CTs the detector is placed in proximity to the sample (Fig. 2-A). This configuration solely measures the imaginary part of the complex refractive index, which is linked to both the absorption and attenuation of X-rays. Essentially, when X-rays pass through material, the attenuation is a result of absorption and scattering phenomena. It can be described by the Lambert-Beer law, where I denotes the intensity measured by the detector, and I_0 the emitted intensity from the X-ray source (see Eq. (2))

$$\ln\left(\frac{I}{I_0}\right) = -\int_0^d \mu(x) dx. \quad (2)$$

The linear attenuation coefficient μ is a function of the material density ρ of the sample, the path length d through the material, the wavelength λ^3 of radiation and the mean atomic number Z^4 . Therefore, given identical measuring conditions, the atomic structure of the sample predominantly determines the resulting attenuation, which is proportional to the imaginary part of the complex refractive index β according to Eq. (3)

$$\mu = 2\pi\beta/\lambda \quad (3)$$

However, absorption is not the only interaction that occurs while X-rays penetrate a sample. Increasing the sample-detector-distance (or placing the sample closer to the source if the detector-source distance is fixed) will cause the intensity image at the detector to include not only attenuation, but also phase shift information. This,

in turn, causes artefacts in the reconstructed images, such as edge enhancement at sample surfaces (both outer and inner) due to small-angle scattering (Fig. 2-B).

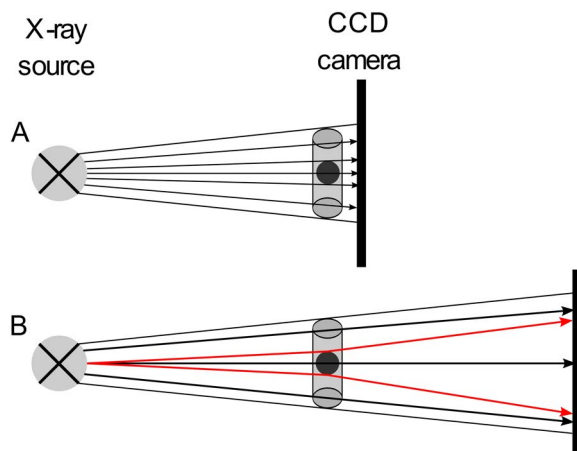


Fig. 2. Different sample-detector-distances; A: classical μ CT, B: phase and attenuation effects mixed (based on (Pacilè and Tromba, 2018)).

This edge enhancement improves the visibility of structural details (Pacilè and Tromba, 2018), but it also makes a threshold-based segmentation impossible. Moreover, to obtain the phase shift information and thus to improve the signal-to-noise-ratio of the reconstructed images, Paganin *et al.* (2002) developed the single-distance phase retrieval algorithm. This algorithm is ap-

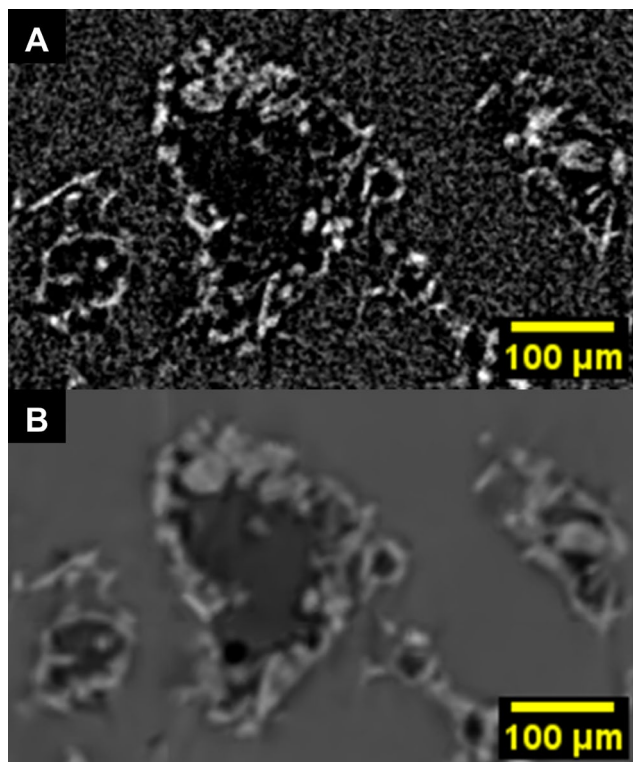


Fig. 3. Comparison between reconstructed images; A: only absorption information, B: with single-distance phase retrieval.

plied to the set of projection images before the reconstruction. The 3D images obtained are phase-contrast images (Fig. 3-B) rather than images based solely on absorption (Fig. 3-A).

This technique, which combines an increased sample-detector distance during the μ CT scan with the application of the single-distance phase retrieval algorithm, is called propagation-based imaging (PBI).

MATERIALS AND METHODS

MATERIALS

Graphite particles (SGB 23 L, AMG Kropfmühl GmbH) are used as the solid phase, water as suspension liquid and highly liquid paraffin oil (Merck KGaA, CAS Nr. 8002-74-2, $\nu = 16 \text{ mm}^2/\text{s}$) as the binding liquid for the spherical agglomeration experiments. The particle size distribution of graphite ranges from $10.9 \mu\text{m}$ to $35.9 \mu\text{m}$ (Fig. 4) and is determined by laser diffraction (Fritsch Analysette 22 MicroTec plus).

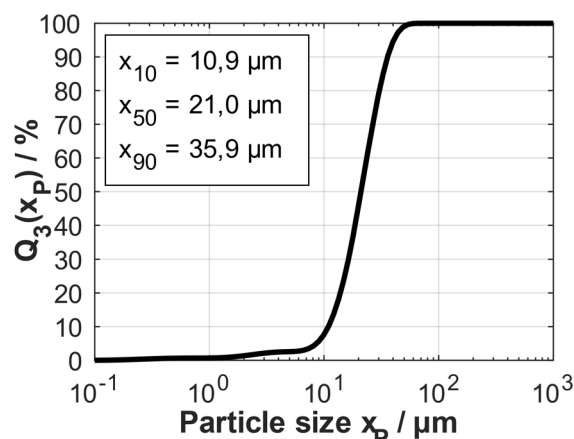


Fig. 4: Graphite particle size distribution; x_{10} , x_{50} and x_{90} are the 10 %, 50 % and 90 % quantile values of the distribution.

The static contact angle of graphite particles in the three-phase system graphite/water/paraffin oil is determined by the method published by Schreier *et. al* (2020). Results showed the static contact angle to be $135^\circ \pm 5.9^\circ$.

SPHERICAL AGGLOMERATION

The spherical agglomeration experiment is carried out in a rheometer (Kinexus Ultra Plus, Netzsch) with a torque measurement accuracy of 0.05 nNm. Within the rheometer, a one-litre vessel with four baffles and an inclined, four-bladed stirrer is mounted on a self-made fixture. 28 g of graphite particles are suspended in 560 g of water ($\beta = 4 \text{ wt.}\%$) for five minutes at a speed of 700 rpm. Additionally, 8.4 g of paraffin oil are emulsified in 140 g of water externally, using a dispersing unit (Ultra Turrax, IKA) at 16000 rpm for two minutes. This results

in a droplet size distribution of $x_{10} = 1.3 \mu\text{m}$, $x_{50} = 14.4 \mu\text{m}$ and $x_{90} = 27.1 \mu\text{m}$. The emulsion is then added to the suspension, and the agglomeration process is initiated with a stirrer speed of 1200 rpm.

SAMPLE PREPARATION FOR μCT

The purpose of the sample preparation is to reduce the mechanical influence on the agglomerates, which consequently would change the morphology, and to avoid sedimentation during the CT scan. Therefore, shock freezing of the samples and scanning them while being cooled in a ‘‘Cryo-Stage’’ is a suitable combination for these requirements. The sample preparation method involves taking samples with a Pasteur pipette of 4 mm inner diameter at one specific time (30 s & 150 s) during the spherical agglomeration experiment. To avoid sedimentation of the agglomerates, they are shock frozen in a mixture of ethanol and dry ice at 195 K for 30 s and then stored in a freezer at 255 K for at least 24 h to complete the crystallisation process (Fig. 5-A).

Following this, about 5 mm of the pipette's height is trimmed (Fig. 5-B) and then positioned on a copper mount (Fig. 5-C). After each of the preparation steps, lasting approximately five seconds, the sample is sprayed with an ice-spray (Cryo-Jet Lamb's Freezing Aerosol, VWR Chemicals) to prevent melting. The copper mount is then inserted into the Cryo-Stage, an additional sample stage that ensures the sample remains frozen throughout the CT scan (Fig. 5-D).

μCT SCAN

A μCT from Bruker (Skyscan 1272) is used for this study. The power of the X-ray source is set to 4.8 W/40 keV with an exposure time of 3000 ms and ro-

tation steps of 0.3° per projection image. The scan position along the z-axis is chosen to be 0.5 mm above the copper pin up to a scan height of 3 mm. Additional scans on another vertical plane are omitted to minimise scan time. This results in a total scan time of approx. 3 h and a resolution of $2.4 \mu\text{m}/\text{voxel}$.

Prior to reconstruction, the projection images are filtered using the Paganin single-distance phase retrieval algorithm described in section Propagation-based X-ray Microtomography, which is implemented by Bruker in their reconstruction software NRecon. Previous internal tests have shown that a ratio of $\delta/\beta = 200$ gives the best results in the following image processing routine.

After the single-distance phase retrieval algorithm, the obtained projection images are getting reconstructed by the software NRecon (Bruker) to obtain a 3D representation of the scanned volume. NRecon uses the Feldkamp algorithm for reconstruction (Feldkamp *et al.*, 1984).

MORPHOLOGICAL PARAMETERS

The morphological parameters are the volume-equivalent sphere diameter x_V , the sphericity according to Wadell Ψ , the fractal dimension D_f according to the Box Counting method and the packing density ρ_{Pack} .

Sphericity

The sphericity according to Wadell (1935) is the ratio between the volume-equivalent sphere diameter x_V and the surface-equivalent sphere diameter x_S raised to the power of 2 (Eq. (4))

$$\Psi = \left(\frac{x_V}{x_S}\right)^2, x_V = \sqrt[3]{\frac{6V}{\pi}}, x_S = \sqrt{\frac{S}{\pi}} \quad (4)$$

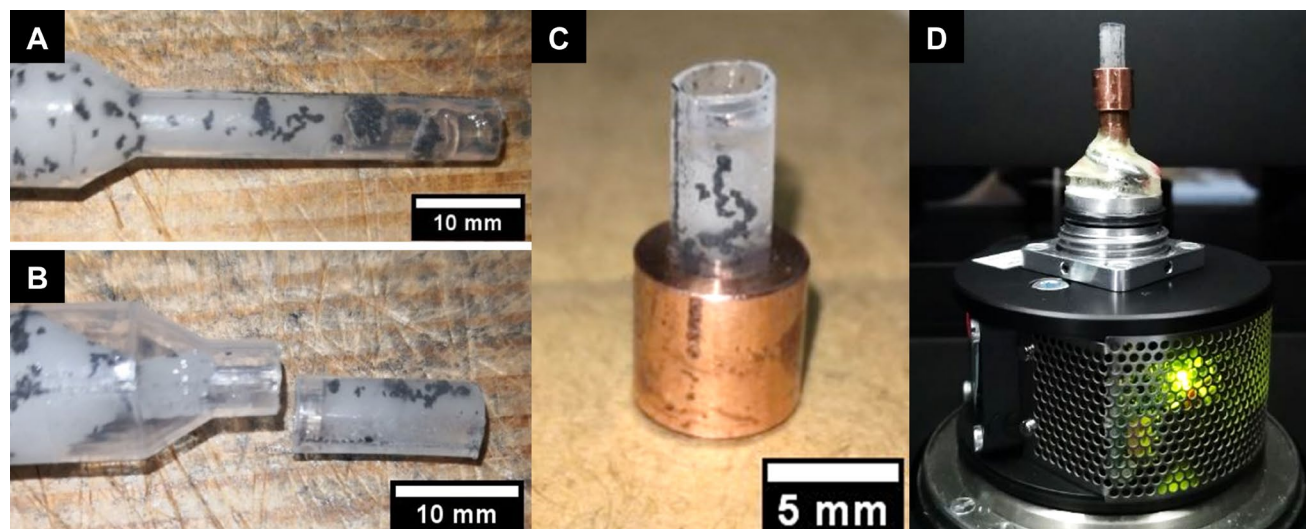


Fig. 5. Sample preparation for X-ray CT; A: Shock-frozen sample out of agglomeration process, B: cut out, C: sample on copper mount, D: Cryo-Stage for Bruker Skyscan 1272.

The volume (V) and surface area (S) of the object are determined and inserted into Eq. (4)

The sphericity lies between $\Psi \in]0,1]$, where a value of 1 represents the perfect sphere and values close to zero represent, for example, a sheet of paper or highly irregularly shaped objects.

Fractal dimension

The fractal dimension is determined by the Box Counting method (Bouligand, 1925). In general, this method is based on an equally spaced grid, which is placed over an object. Then all squares (2D) or cubes (3D) that cover one piece of the object are counted. Then the box size is increased and the counting is repeated. The data points box size (L) and number of object boxes (N(L)) are plotted against each other in a log-log plot (see Fig. 6). In this study the Box Counting algorithm is implemented by the MatLab function `boxcount` written by Moisy (2022). In this function the box size L is scaled to the power of two.

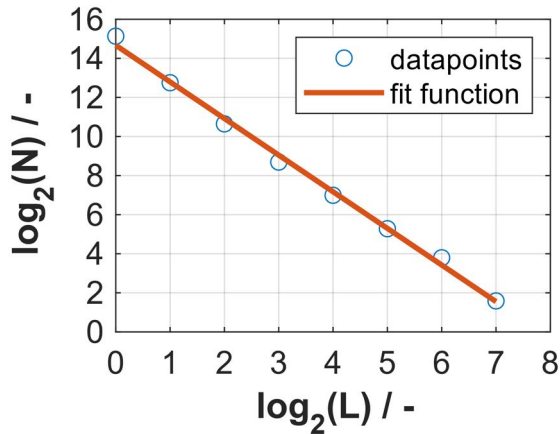


Fig. 6. Number of surface voxels dependent on the box size during the Box Counting method.

The absolute value of the slope then represents the fractal dimension (see Eq. (5))

$$D_f = \lim_{L \rightarrow \infty} \frac{\log(N(L))}{\log(1/L)} \quad (5)$$

According to this definition, the fractal dimension falls within the range of $D_f \in [1,3]$ and is equivalent to the space dimension for typical geometric objects. For instance, a perfect solid sphere has a fractal dimension of 3.

Packing density

The packing density $\rho_{\text{Pack}} \in [0,1]$ is a measure of the compactness of an object consisting of several small objects (Gupta and Larson, 1979). When this principle

is applied to agglomerates obtained by spherical agglomeration, the space-filling objects are represented by the solid particles, and the total volume is the convex hull volume of the agglomerate (see Eq. (6)).

$$\rho_{\text{Pack}} = \frac{V_{\text{Particles}}}{V_{\text{convex hull}}} \quad (6)$$

TWO-DIMENSIONAL KERNEL DENSITY DISTRIBUTION

The result of the image post-processing and analysis mentioned later is object discrete data, since all the parameters mentioned in the Morphological Parameters section are known for each individual object. In such a case the probability density distributions can be calculated using kernel density estimation, which were first introduced by Parzen (1962). The advantage of kernel density estimation is that no assumption is made about the distribution of the data. Schach *et al.* (2019) used two-dimensional kernel estimations in the context of mineral processing to calculate the two-dimensional distributions, where the probability $\hat{f}_{xy}(x,y)$ is determined using two particle properties x and y

$$\hat{f}_{xy}(x,y) = \sum_{i=1}^n \frac{1}{n} * \kappa_x \left(\frac{x-x_i}{b_x} \right) * \kappa_y \left(\frac{y-y_i}{b_y} \right). \quad (7)$$

In Eq. (7) b_x and b_y represent the bandwidth of the kernels κ_x and κ_y , whereas κ_y represents the sample size. In the used MatLab script the function `ksdensity` (Peter D., 1985; Silverman, 1986; Bowman and Azalini, 1997) is used to calculate the two-dimensional kernel estimation.

IMAGE POST-PROCESSING

The aim of the image post-processing is to obtain a representation of each individual agglomerate (particles plus binding liquid) within the scanned volume. The morphological parameters volume-equivalent sphere diameter, sphericity, fractal dimension and packing density are then computed.

IMAGE PROCESSING & ANALYSIS ROUTINE

The image processing & analysis routine and the computation of the morphometric parameters are carried out in a self-written script based on MatLab (R2022a) together with the toolboxes *Image Processing*, *Statistics & Machine Learning* and *Curve Fitting*. The individual steps of the image processing routine are described below. The image processing operations used are in italics. The MatLab commands are given in brackets to make the whole implementation easier for the reader.

As a first step, the reconstructed images (Fig. 8-A) are filtered with a *Non-Local Means Denoising* (*imnlm-filt*) algorithm (Fig. 8-B) (Buades *et al.*, 2011). Compared to other filters such as *Gaussian Blur* or *Median*, the *Non-Local Means Denoising* requires more computation time, but has the advantage of preserving edges and boundaries. Next, the *Gradient* (*imggradient3*) is applied which calculates the directional change in the grey scale values within an image using the Sobel operator (Tennenbaum *et al.*, 1969). When a *Threshold* (*otsuthresh*) (Otsu, 1979) is applied to the result of the *Gradient*, the boundaries of the microagglomerates are binarised (Fig. 8-C). The advantage of segmenting the boundaries with the combination of *Gradient* and *Threshold* is the shape-independent binarisation of the outer contour and thus the preservation of the original object shape.

Since the contour of the agglomerate is formed by particles and is therefore not completely closed, it is filled in a two-step process. First, the binding liquid must be added to the contour, because at this early stage of agglomeration, the droplets of binding liquid are covered with particles. To achieve this, the binding liquid is segmented in the original images via *Threshold*. In this case the *Threshold* was set between the two peaks of the gray value histogram shown in Fig. 7, where the first peak corresponds to the binding liquid and the second peak to the matrix.

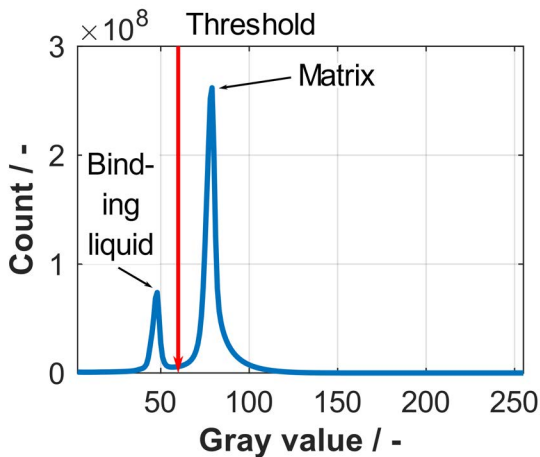


Fig. 7. *Grey value histogram of the whole 3D volume.*

Secondly, any remaining holes are closed using a *3D Fill Holes* (*imfill*) (Soille and Ansout, 1990) algorithm. The result of these operations is a segmented representation of the agglomerates (Fig. 8-D).

In the experiment discussed in section Spherical Agglomeration, the samples are taken at the beginning of the agglomeration process. In this case, the agglomerates are still small and there is a high number concentration of objects in the scanned volume. Consequently,

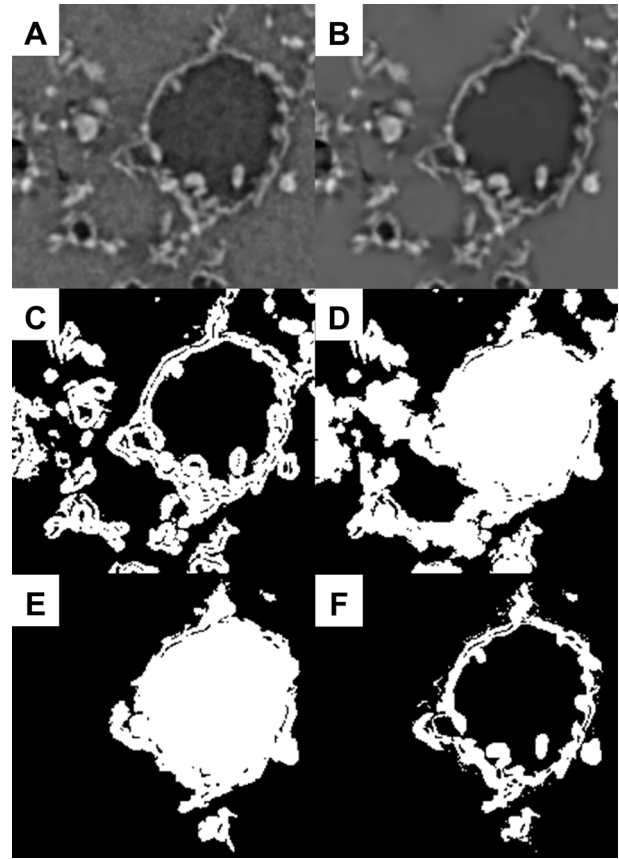


Fig. 8. *Image processing; A: original image, B: image after applying Non-Local Means Denoising, C: agglomerate contour after applying Gradient and Threshold, D: filled agglomerate with segmented binding-liquid, E: single agglomerate after applying the Distance Transform Watershed, F: particle volume of the corresponding agglomerate from image E.*

the distance between two objects can be very small (only a few voxels), resulting in a mixed grey value between the matrix and the object. This CT artefact is called Partial Volume Effect (PVE) (Buzug, 2008). Due to this mixed grey value, the objects appear to be connected after segmentation. To overcome this problem, a *Distance Transform Watershed* is computed to separate the objects from each other.

The main steps of this set of algorithms are as follows: For all segmented objects the so-called *Distance Transform* (*bwdist*) (Rosenfeld and Pfaltz, 1966; Paglieroni, 1992) is computed. This algorithm assigns each voxel a number representing the distance between that voxel and the nearest non-zero voxel resulting in the highest value at the centroid of the object. Multiplying the output of the distance transform by -1 produces a set of minima marker which is consequently the basis for the flooding algorithm of the *Watershed Transform* (*watershed*) (Meyer, 1994). Due to the *Distance Transform*, an object may contain more than one minimum, leading

to over-segmentation in the *Watershed Transform*. Applying an *H-minima Transform* (*imhmin*) (Schmitt and Prêteux, 1986) to the *Distance Transform* reduces the number of minima and therefore the over-segmentation (Ismail *et al.*, 2016) (Fig. 8-E).

All image operations mentioned so far are computed on the whole image stack. From now on, all further image processing steps are computed on each individual object detected by the *Distance Transform Watershed*.

After the segmentation of individual agglomerates, the parameters volume, surface area, sphericity and fractal dimension are determined. As mentioned in section Morphological Parameters, the particle volume and the convex hull volume must be calculated to determine the packing density. This is done by computing the *Bounding Box* (*regionprops3*), which is the smallest cuboid aligned with the coordinates containing the segmented region (The MathWorks Inc., 2022). The same region is cropped in the original filtered images. After applying the crop, the same *Threshold* for the binding liquid is set as at the beginning, so that the binding liquid is segmented again. This binding liquid volume corresponding to this individual agglomerate is then subtracted from the agglomerate image stack, resulting in an indi-

vidual particle volume representation (Fig. 8-F).

QUALITATIVE EVALUATION OF IMAGE PROCESSING ROUTINE

The *Distance Transform Watershed* segmentation described earlier has a major impact on the results of image processing. Over-segmentation (one object is separated into two or even more objects) can be reduced by applying an *H-minima Transform*, but there are still cases where the segmentation does not represent the original object. As shown in Fig. 9, three distinct cases have been selected from a large pool of objects. Fig. 9-A depicts a highly branched agglomerate that has been segmented into three smaller ones. The original objects correlate well with the segmented objects. This also applies to the nearly spherical agglomerates illustrated in Fig. 9-B. The third case displays an elongated agglomerate formed by numerous primary particles and small agglomerates. The segmentation divides this agglomerate into three parts, as seen in Fig. 9-C. This is a case of persistent over-segmentation. Varying the values in the *H-minima transform* did not alter this over-segmentation. Consequently, we conducted a manual clean-up of the data by inspecting each segmented object after analysis and comparing the segmentation result with the original object.

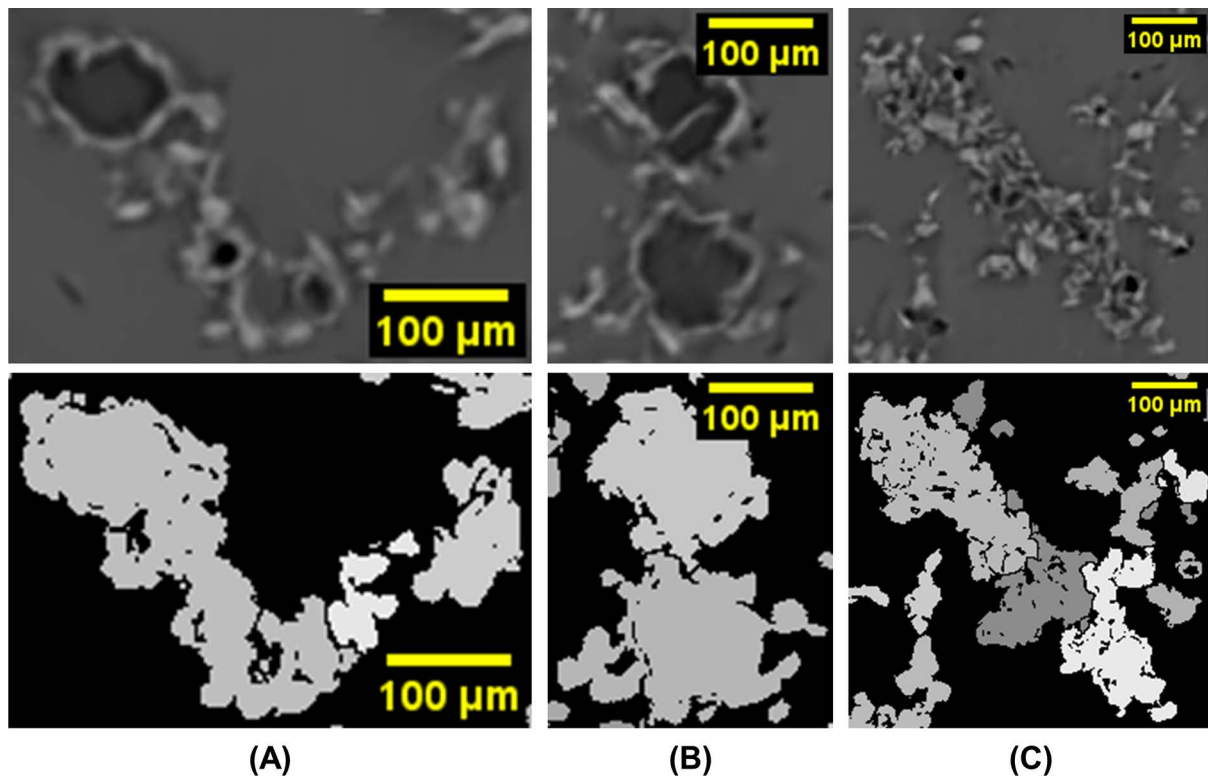


Fig. 9: Original object and corresponding segmentation result after applying *Distance Transform Watershed*; A: good segmentation of branched agglomerates, B: good segmentation of nearly spherical agglomerates, C: over segmentation of elongated agglomerates.

RESULTS AND DISCUSSION

Using the image post-processing routine, 2420 agglomerates could be detected after 30 s agglomeration time and only 85 after 150 s. For each agglomerate, the parameters volume equivalent sphere diameter, sphericity, fractal dimension and packing density, are calculated according to section Morphological Parameters. The concentration of agglomerates decreases significantly over time. Therefore, the data corresponding to 150 s are presented as averages with minimum and maximum values.

The first parameters evaluated are the volume-equivalent sphere diameter of the agglomerates x_{VA} and the size of the paraffin content x_{VP} within them. The cumulative number distribution $q_0(x_{VA}, x_{VP})$ of both sizes shows that the whole agglomerate size ranges between $57 \mu\text{m}$ and $362 \mu\text{m}$, whereas the paraffin size ranges between $4 \mu\text{m}$ and $242 \mu\text{m}$ (see Fig. 10-A). Evidently, when the two-dimensional number distribution of both sizes is determined, large agglomerate sizes correlate with large paraffin droplet sizes and vice versa (see Fig. 10-B).

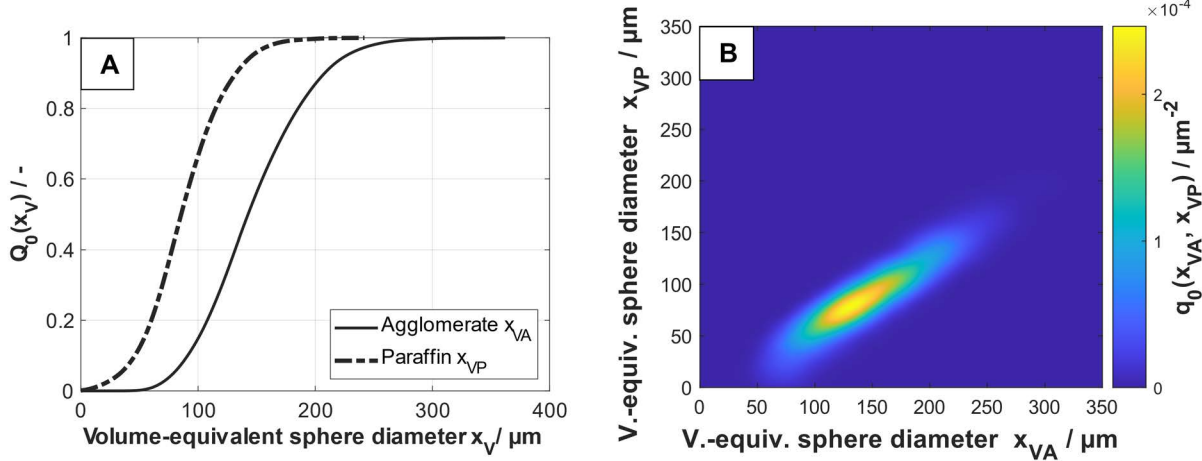


Fig. 10: Size distribution; A: cumulative number distributions of whole agglomerate and paraffin droplet inside agglomerate, B: two-dimensional number density distribution of agglomerate size and paraffin droplet size.

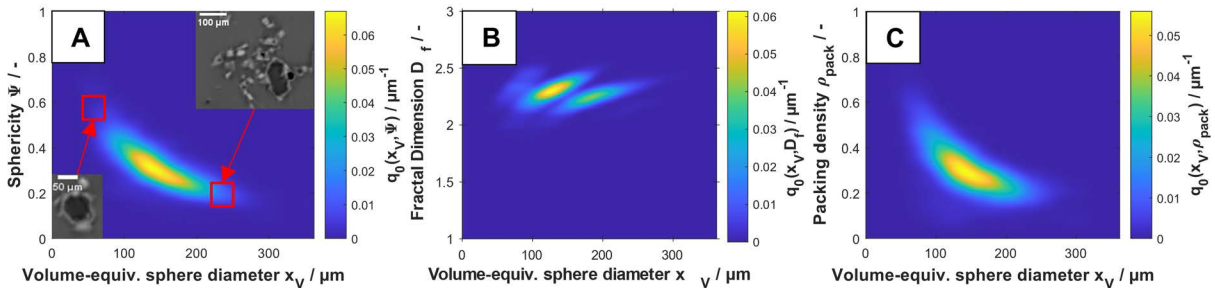


Fig. 11. Two-dimensional number density distribution of volume-equivalent sphere diameter and corresponding morphological parameter; A: sphericity, B: fractal dimension, C: packing density.

The sphericity, fractal dimension and packing density of the agglomerates are size dependent, as can be seen in Fig. 11. In particular, the smaller agglomerates between $50 \mu\text{m}$ and $100 \mu\text{m}$ show higher sphericity values from 0.5 to 0.8 (Fig. 11-A), lower fractal dimensions of about 2.1 (Fig. 11-B) and higher packing densities between 0.6 and 0.8 (Fig. 11-C). This indicates that smaller agglomerates contain small paraffin droplets with only a single layer of particles at the surface, as highlighted in the lower left of Fig. 11-A. The high sphericity values and the low fractal dimensions tend towards perfect spheres ($\Psi = 1$, $D_f = 3$), but the agglomerate surface area is increased due to the particles at the droplet surface. In addition, these small agglomerates also have high packing densities, because the convex hull is only slightly different from the agglomerate itself and the particle content is also high.

The parabolic shape of $q_0(x_V, \Psi)$ (Fig. 11-A) was expected because the sphericity Ψ is directly related to the volume-equivalent sphere diameter x_V according to Eq. (4).

In contrast, larger agglomerates between 150 μm and 300 μm have low sphericity values ($0.1 < \Psi < 0.3$) and low packing densities ($0.1 < \rho_{\text{Pack}} < 0.3$). Consequently, larger agglomerates show complex structures (see Fig. 11-A top right) which are more interconnected and therefore have a larger surface area compared to smaller agglomerates. This increased surface area leads to the second peak in the fractal dimension (see Fig. 11-B) and to a decrease in the sphericity. Moreover, the convex hull volume of this interlinked structures is also high, leading to a decrease in the calculated packing density.

In addition to the two-dimensional distributions depending on the volume-equivalent sphere diameter, Fig. 12 shows the correlation between the packing density and the sphericity. It can be observed that low values of sphericity correlate with low values of packing density and vice versa. Additionally, the data lie along the bisector line, which shows that both packing density and sphericity are influenced in the same way by the increased surface area of the interconnected agglomerates. This trend is also seen in the sample taken after 150 s of agglomeration. Whether this is the case throughout the agglomeration process will have to be verified again.

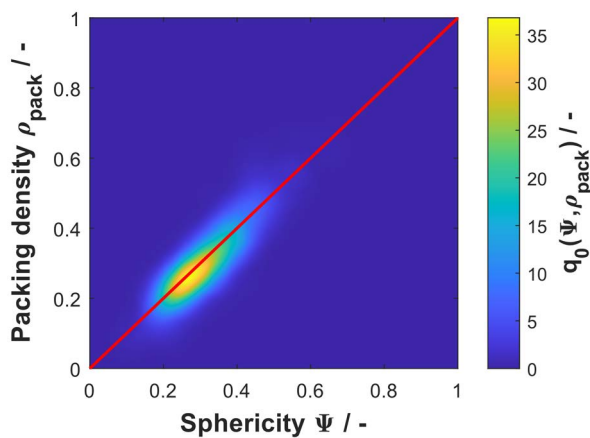


Fig. 12. Two-dimensional number density distribution of sphericity and packing density (red line represents the bisector line).

All results so far have been obtained from the sample taken after 30 s agglomeration time. If we compare these with the results after 150 s agglomeration time, we see an increase in the volume equivalent sphere diameter to $x_{50,150s} = 260 \mu\text{m}$ ($x_{\text{min}} = 113 \mu\text{m}$ & $x_{\text{max}} = 472 \mu\text{m}$), which is larger than $x_{50,30s} = 146 \mu\text{m}$. Furthermore, the packing density, as well as the sphericity and the fractal dimension all show higher values compared to the 30 s agglomeration time ($\rho_{\text{Pack},50} = 0.45$, $\Psi_{50} = 0.55$, $D_{f,50} = 2.45$). This indicates that the agglomerates become more

packed and more spherical during spherical agglomeration. Other authors, such as Blandin *et al.* (2003) and Müller & Löffler (1996), have also reported this effect where agglomerates begin with more interconnected and complex structures, but become more spherical and compact during agglomeration.

CONCLUSION

The aim of this paper was to present a method that can be used to study the morphology of agglomerates during the agglomeration process. It has been demonstrated that the combination of shock freezing a sample in an ethanol-dry ice mixture, which prevents sedimentation of the suspended agglomerates, in combination with the propagation-based X-ray microtomography is suitable to study the morphology of agglomerates generated by the spherical agglomeration process.

The first results of the morphological parameters (volume-equivalent sphere diameter, sphericity, fractal dimension and packing density) show that the size of the agglomerates at the beginning of the process is directly related to the paraffin droplet size inside the agglomerates. Furthermore, the values of sphericity, fractal dimension and packing density are size dependent in samples evaluated, while the fractal dimension shows a second peak when agglomerates consist of many linked particles.

In the future, this methodology will be applied to study the time-dependent morphology of agglomerates during the spherical agglomeration process over the three different process phases.

ACKNOWLEDGMENTS

This work was supported by the German Research Foundation (DFG) [grant number: BR 1151/8-1].

REFERENCES

- Bemer GG (1979). Agglomeration in Suspension: A Study of Mechanisms and Kinetics. Delft University of Technology the Netherlands.
- Blandin AF, Mangin D, Rivoire A, Klein JP, Bossoutrot JM (2003). Agglomeration in suspension of salicylic acid fine particles: influence of some process parameters on kinetics and agglomerate final size. Powder Technol 130:316–23.
- Bos AS (1983). Agglomeration in Suspension. Delft University of Technology the Netherlands.
- Bouligand G (1925). Dimension, 'etendue, densité'. Comptes Rendus Acad Sci 180:245–8.
- Bowman AW, Azzalini A (1997). Applied Smoothing Techniques for Data Analysis. New York: OUP Oxford.

- Buades A, Coll B, Morel JM (2011). Non-Local Means Denoising. *Image Process Line* 1:208–12.
- Buzug TM (2008). *Computed tomography From photon statistics to modern cone-beam CT*. Berlin Heidelberg:Springer. 522 pp.
- Cattermole AE (1904). Classification of the metallic constituents of ores. US Patent 763259.
- Dawei W, Kewu W, Jicun Q (1986). Hydrophobic agglomeration and spherical agglomeration of wolframite fines. *Int J Miner Process* 17:261–71.
- Dioguardi F, Mele D, Dellino P, Dürig T (2017). The terminal velocity of volcanic particles with shape obtained from 3D X-ray microtomography. *J Volcanol Geoth Res* 329:41–53.
- Dosta M, Bröckel U, Gilson L, Kozhar S, Auernhammer GK, Heinrich S (2018). Application of micro computed tomography for adjustment of model parameters for discrete element method. *Chem Eng Res Des* 135:121–8.
- Drzymala J, Markuszewski R, Wheelock TD (1991). Oil Agglomeration of Sulfurizes Pyrite. *Miner Eng* 4:161–72.
- Feldkamp LA, Davis LC, Kress JW (1984). Practical cone-beam algorithm. *J Opt Soc Am A* 1:612–9.
- Gilson L, Bröckel U (2015). Einsatz von Bilderkennung zur Auswertung tomographischer Aufnahmen für die Erfassung von Partikelformen. *Chem-Ing-Tech* 87:986–90.
- Guo S, Yu C, Feng S, Wei J, Tong L, Li K, Gao Y, Zhao P, Li T, Chen M, Han D, Gong J (2022). Enabling the drug combination of celecoxib through a spherical co-agglomeration strategy with controllable and stable drug content and good powder properties. *Int J Pharm* 626:122180.
- Gupta SC, Larson WE (1979). A Model for Predicting Packing Density of Soils Using Particle-Size Distribution. *Soil Sci Soc Am J* 43:758–64.
- House CI, Veal CJ (1989). Selective recovery of chalcopyrite by spherical agglomeration. *Miner Eng* 2:171–84.
- Ismail NHF, Mohd Zaini TR, Jaafar M, Che Pin N (2016). H-minima transform for segmentation of structured surface. *MATEC Web Conf* 74:00025.
- Kardos A, Tóth J, Trif L, Gyenis J, Feczko T (2016). Preparation of spherical agglomerates from potash alum. *Rsc Adv* 6:5466–73.
- Kawashima Y, Capes CE (1974). An experimental study of the kinetics of spherical agglomeration in a stirred vessel. *Powder Technol* 10:85–92.
- Kawashima Y, Capes CE (1976). Further studies of the kinetics of spherical agglomeration in a stirred vessel. *Powder Technol* 13:279–88.
- Kawashima Y, Takagi H, Takenaka H (1981). Wet spherical agglomeration of binary mixtures II: Mechanism and kinetics of agglomeration and the crushing strength of agglomerates. *Chem Pharm Bull* 29:1403–9.
- Kelsall GH, Pitt JL (1987). Spherical agglomeration of fine wolframite ((Fe,Mn)WO₄) mineral particles. *Chem Eng Sci* 42:679–88.
- Leißner T, Diener A, Löwer E, Ditscherlein R, Krüger K, Kwade A, Peuker UA (2019). 3D ex-situ and in-situ X-ray CT process studies in particle technology – A perspective. *Adv Powder Technol* 31:78–86.
- Meyer F (1994). Topographic distance and watershed lines. *Signal Process* 38:113–25.
- Miller JD, Lin CL (2004). Three-dimensional analysis of particulates in mineral processing systems by cone beam X-ray microtomography. *Miner Metall Proc* 21:113–24.
- Moisy F (2022). boxcount. Retrieved May 9, 2022, from <https://www.mathworks.com/matlabcentral/fileexchange/13063-boxcount>.
- Müller M, Löffler F (1996). Development of Agglomerate Size and Structure during spherical agglomeration in suspension. *Part Part Syst Char* 13:322–6.
- Otsu N (1979). A Threshold Selection Method from Gray-Level Histograms. *IEEE T Syst Man Cyb* 9:62–6.
- Pacilè S, Tromba G. (2018). Introduction to X-Ray Microtomography. In: Giuliani A, Cedola A, eds. *Advanced High-Resolution Tomography in Regenerative Medicine, Fundamental Biomedical Technologies*. Ch. 2. Cham:Springer International Publishing, 19–39.
- Paganin D, Mayo SC, Gureyev TE, Miller PR, Wilkins SW (2002). Simultaneous phase and amplitude extraction from a single defocused image of a homogeneous object. *J Microsc* 206:33–40.
- Paglieroni DW (1992). Distance transforms: Properties and machine vision applications. *CVGIP-Graph Model Im* 54:56–64.
- Parzen E (1962). On Estimation of a Probability Density Function and Mode. *Ann Math Stat* 33:1065–76.
- Pashminehazar R, Ahmed SJ, Kharaghani A, Tsotsas E (2018). Spatial morphology of maltodextrin agglomerates from X-ray microtomographic data: Real structure evaluation vs. spherical primary particle model. *Powder Technol* 331:204–17.
- Pashminehazar R, Kharaghani A, Tsotsas E (2016). Three dimensional characterization of morphology and internal structure of soft material agglomerates produced in spray fluidized bed by X-ray tomography. *Powder Technol* 300:46–60.
- Petela R, Ignasiak B, Pawlak W (1995). Selective agglomeration of coal: analysis of laboratory batch test results. *Fuel* 74:1200–10.

- Peter D (1985). Kernel estimation of a distribution function. *Commun Stat-Theor M* 14:605–20.
- Rosenfeld A, Pfaltz JL (1966). Sequential Operations in Digital Picture Processing. *J ACM* 13:471–94.
- Schach E, Buchmann M, Tolosana-Delgado R, Leißner T, Kern M, Van den Boogaart G, Rudolph M, Peuker UA (2019). Multidimensional characterization of separation processes – Part 1: Introducing kernel methods and entropy in the context of mineral processing using SEM-based image analysis. *Miner Eng* 137:78–86.
- Schmitt, M., Prêteux, F. (1986). Un nouvel algorithme en morphologie mathématique: les rh maxima et rh minima. *Proc 2ieme Sem Int Image Electron* 469–75.
- Schreier J, Bröckel U (2021). Multidimensional separation due to selective spherical agglomeration—Evidence of shape separation via X-ray microtomography. *Particology* 58:316–23.
- Schreier J, Furat O, Cankaya M, Schmidt V, Bröckel U (2020). Automated Evaluation of Contact Angles in a Three-Phase-System of Selective Spherical Agglomeration. *Image Anal Stereol* 39:179–88.
- Silverman BW (1986). *Density Estimation for Statistics and Data Analysis*. Boca Raton: CRC Press.
- Sirianni AF, Capes CE, Puddington JE (1969). Recent experience with the spherical agglomeration process. *Can J Chem Eng* 47:166–70.
- Soille PJ, Ansoult MM (1990). Automated basin delineation from digital elevation models using mathematical morphology. *Signal Process* 20:171–82.
- Tennenbaum J, Kay A, Binford T, Falk G, Feldman J, Grape G, Pau R, Pingle K (1969). The sobel edge detector, Proceedings of the First International Joint Conference on Artificial Intelligence, 1969 May 7-9; Washington DC, United States.
- Thati J, Rasmuson AC (2012). Particle engineering of benzoic acid by spherical agglomeration. *Eur J Pharm Sci* 45:657–67.
- The MathWorks Inc (2022). Measure properties of 3-D volumetric image regions - MATLAB regionprops3. Retrieved January 31, 2022, from https://www.mathworks.com/help/images/ref/regionprops3.html#mw_ed79d5ec-5aa3-4a85-a8a0-0a0e65720ef2.
- Wadell H (1935). Volume, Shape, and Roundness of Quartz Particles. *J Geol* 43: 250–80.
- Wahl EF, Baker CGJ (1971). The kinetics of titanium dioxide agglomeration in an agitated liquid suspension. *Can J Chem Eng* 49:742–6.